RESEARCH ARTICLE

ADVANCED
MATERIALS
TECHNOLOGIES

www.advmattechnol.de

Check for updates

Wafer-Scale Gold Nanomesh via Nanotransfer Printing toward a Cost-Efficient Multiplex Sensing Platform

Min Gao, Yi-Bo Zhao, Zhi-Jun Zhao,* Guangyu Qiu,* Yile Tao, Guochen Bao, Ying Du, Martin Spillmann, Jiukai Tang, Soonhyoung Hwang, Jun-Ho Jeong, and Jing Wang*

Multiplex sensing platforms via large-scale and cost-efficient fabrication processes for detecting biological and chemical substance are essential for many applications such as intelligent diagnosis, environmental monitoring, etc. For the past decades, the performance of those sensors has been significantly improved by the rapid development of nanofabrication technologies. However, facile processes with cost-effectiveness and large-scale throughput still present challenges. Nano-transfer printing together with the imprinting process shows potential for the efficient fabrication of 100 nm structures. Herein, a wafer-scale gold nanomesh (AuNM) structure on glass substrates with 100 nm scale features via nano-imprinting and secondary transfer printing technology is reported. Furthermore, potential sensing applications are demonstrated towards biochemical substance detection by using AuNM structures as highly responsive substrates for achieving the surface enhanced Raman spectroscopy (SERS), and as working electrodes of electrochemical analysis for the detection of metallic ions. In the SERS detection mode, different nucleotides can be detected down to 1 nM level and distinguished via their unique fingerprint patterns. As for electrochemical analysis mode, Pb^{2+} ions can be detected out of other interfering components with concentration down to 30 nM. These multimodal sensing mechanisms provide complementary information and pave the way for low-cost and high-performance sensing platforms.

1. Introduction

In recent decades, rapid development of industrialization and digitalization for the oncoming era of internet of things (IoTs) puts an emerging demand for smart sensors to selectively and sensitively detect chemical and biological substances toward various application scenarios such as wearable electronics, intelligent point-of-care (POC) diagnosis, environmental monitoring, etc.[1,2] To meet those emerging requirements properly, ideal biochemical sensors should possess properties such as high sensitivity, long-term robustness, fast response, real-time monitoring capability, excellent selectivity, low unit cost, lower limit of detection, wide dynamic range, low power consumption, etc.[3] However, human beings still need a journey of steep climbing to achieve these goals. Notably, the global pandemic of coronavirus disease 2019 (Covid-19) exposed that our technology reserve is not well prepared in meeting such urgent, massive and versatile requirement, and aroused tremendous attention on biochemical sensing technologies.

To date, several major technology routes, including chemoresistive,[4,5] plasmonic,[6,7] electrochemical,[8,9] acoustic sensors,[10,11] etc. have been developed and each of those sensors shows specific merits on certain abovementioned aspects toward various real application scenarios. The rapid development of nanofabrication technologies for different materials and various structures has dramatically enhanced the performance of those sensing devices due to their small features and active structural properties such as high surface-to-volume ratios, unique physical properties, etc.[12–14]

M. Gao, Y.-B. Zhao, Y. Tao, M. Spillmann, J. Tang, J. Wang
Institute of Environmental Engineering
ETH Zürich, Zürich 8093, Switzerland
E-mail: jing.wang@ifu.baug.ethz.ch

M. Gao, Y.-B. Zhao, J. Tang, J. Wang
Laboratory for Advanced Analytical Technologies
Empa
Swiss Federal Laboratories for Materials Science and Technology
Dübendorf 8600, Switzerland

The ORCID identification number(s) for the author(s) of this article can be found under https://doi.org/10.1002/admt.202201758.

Z.-J. Zhao
Institute of Smart City and Intelligent Transportation
Southwest Jiaotong University
Chengdu 611756, China
E-mail: zhaozhijun@swjtu.edu.cn

G. Qiu
Institute of Medical Robotics
School of Biomedical Engineering
Shanghai Jiao Tong University
Shanghai 200240, China
E-mail: guangyuqiu@sjtu.edu.cn

G. Bao, Y. Du
College of Science
Zhejiang University of Technology
Hangzhou 310023, China

S. Hwang, J.-H. Jeong
Nano-Convergence Mechanical Systems Research Division
Korea Institute of Machinery and Materials
Daejeon 34103, South Korea

**ADVANCED
SCIENCE NEWS**

www.advancedsciencenews.com

**ADVANCED
MATERIALS
TECHNOLOGIES**

www.advmattechnol.de

Therefore, fabrication technologies, which can repeatably and cost-efficiently produce structures with sub-100-nm features are of significant importance for promoting the wide applications of those biochemical sensors.

Fabrication processes that follow the traditional top–down route and generally couple with the CMOS process, produce structures with excellent uniformity and repeatability.[15] However, conventional UV lithography shows its limit down to 1 µm scale structures, while expensive and time-consuming processes like extreme UV (EUV) or electron beam lithography (EBL) are needed to achieve structures within the nanometer range.[16] Bottom-up methods show high yield for producing nanoscale structures with low cost. However, the structural repeatability and facile process of device integration still need to be improved.[17] Several novel methods utilizing the self-assembled nanostructure including block-copolymer (BCP) lithography, nanosphere (NP) lithography are proposed to be able to produce sub-10-nm-scale structures, but mass-production in large-area is still an essential issue to be solved for those methods.[18–20] Therefore, facile processes with cost-effectiveness and high throughput still present challenges.

Nanoimprinting lithography (NIL), as an alternative choice, exhibits potential in solving those issues such as high fabrication cost and long processing time. Meanwhile, it offers promising features of well-designed patterns with good uniformity over large area, and facile mass-production, especially for 100-nm-scale metallic structures.[21–24] Additionally, diverse novel structures available from NIL enable different mechanisms to be utilized complementarily and even synergistically, which, thus, can further enhance the sensing performance of these devices.[25,26]

In this work, we report wafer-scale, uniformly patterned gold nanomesh (AuNM) structures on glass substrates with 100-nm scale features via nanoimprinting and secondary chemisorption-assisted transfer printing technology. We further demonstrate potential sensing applications toward biochemical substance detection by using these AuNM structures as highly responsive substrates for achieving the surface enhanced Raman spectroscopy (SERS), and as working electrodes of electrochemical analysis for detection of metallic ions. In SERS sensing mode, different nucleotides can be detected down to 1 nM level and distinguished via their unique fingerprint patterns. As for electrochemical analysis mode, Pb^{2+} ions can be detected out of other interfering components with the concentration down to 30 nM. As an optical analytical method, SERS provides fingerprint identification of the analytical molecules in a label-free and nondestructive way. On the other hand, electrochemical methods can be responsive to metallic analytes without Raman scattering effects. These multimodal sensing mechanisms provide complementary information and the strategy may pave the way for future low-cost, high-performance, and highly integrated optoelectronic sensors for detection of chemical and biological substances.

2. Results and Discussion

2.1. Wafer-Scale Fabrication and Characterization of AuNM

The fabrication process of the AuNM via nanoimprinting and transfer is schematically illustrated in **Figure 1**a. The soft template is inversely replicated from the silicon master mold with 100-nm scale features, which is initially fabricated by the krypton fluoride (KrF) lithography process. A gold layer is then deposited on the soft template to form the initial nanopatterns. Following that, the prepared gold patterns on the surface of the soft template are directly transferred onto the glass wafer-receiving substrate, under the pressure of 5 bar and temperature of 160 °C with assistance of chemical adhesion layers, to form the AuNM structures on glass directly. After cooling down, the AuNM on the surface of the soft mold is detached from the mold and stay on the glass substrate. Chemical-free nanotransferring process can also be enabled by the chemisorption between the Au and glass substrate under the external heat and pressure.[22] However, the uniformity will be impaired when coming to the thicker Au-layer transferring process.[27] Therefore, considering the fact that additional chemical adhesion layer has no impact on our target applications, the chemical adhesion layer is employed in our fabrication process. Figure 1b shows the photograph of the fabricated AuNM on a 6-inch glass substrate with four different patterns, indicating excellent uniformity of the gold pattern with 100-nm scale features on the glass substrate in large areas from a macroview of the transfer printing method, which, to the best of our knowledge, has been rarely reported so far. Theoretically, the ultimate fabrication precision of NIL depends on the feature of the template. In general, templates with smaller features give finer imprinted structures. Sub-10-nm templates can be fabricated by using EBL and photolithography techniques. However, the smaller size leads to difficulties on the transfer process. So far, we can successfully perform the transfer process with sub-100-nm features with high yield. Direct transfer of structures with smaller sizes was not tried yet, which, however, is a worthwhile challenge to overcome further. Regarding the uniformity at a microscale, the SEM images of relatively large area and a close-up view of the AuNM at region 2 are shown in Figure 1c,d, respectively. The X-ray diffraction (XRD) pattern shown in Figure S1 (Supporting Information) indicates distinct peaks at 38.1, 44.3, and 64.5 degrees, which correspond to standard Bragg reflections (111), (200), and (220) of face center cubic (fcc) lattice. The characteristic colors of the four regions are induced by the different plasmonic effect of the periodic dimensions in those areas. The SEM images of each region are also illustrated in Figure S2 (Supporting Information) and the ultraviolet–visible (UV–Vis) spectroscopy of those samples are shown in Figure S3 (Supporting Information) as the supplementary characterizations of those fabricated AuNM on the glass substrate, exhibiting the wide-range tunability of the optical properties by our methods. Moreover, an image showing the structure and the corresponding element mappings consisting of gold, silicon, and oxygen are exhibited in Figure 1e–h, which further confirms the elemental information of the fabricated AuNM.

2.2. Standard Characterization of AuNM as SERS Substrates

To exemplify the applicability of the fabricated AuNM structures toward biochemical sensing, we first demonstrate their potential application as SERS substrates, where nanostructures
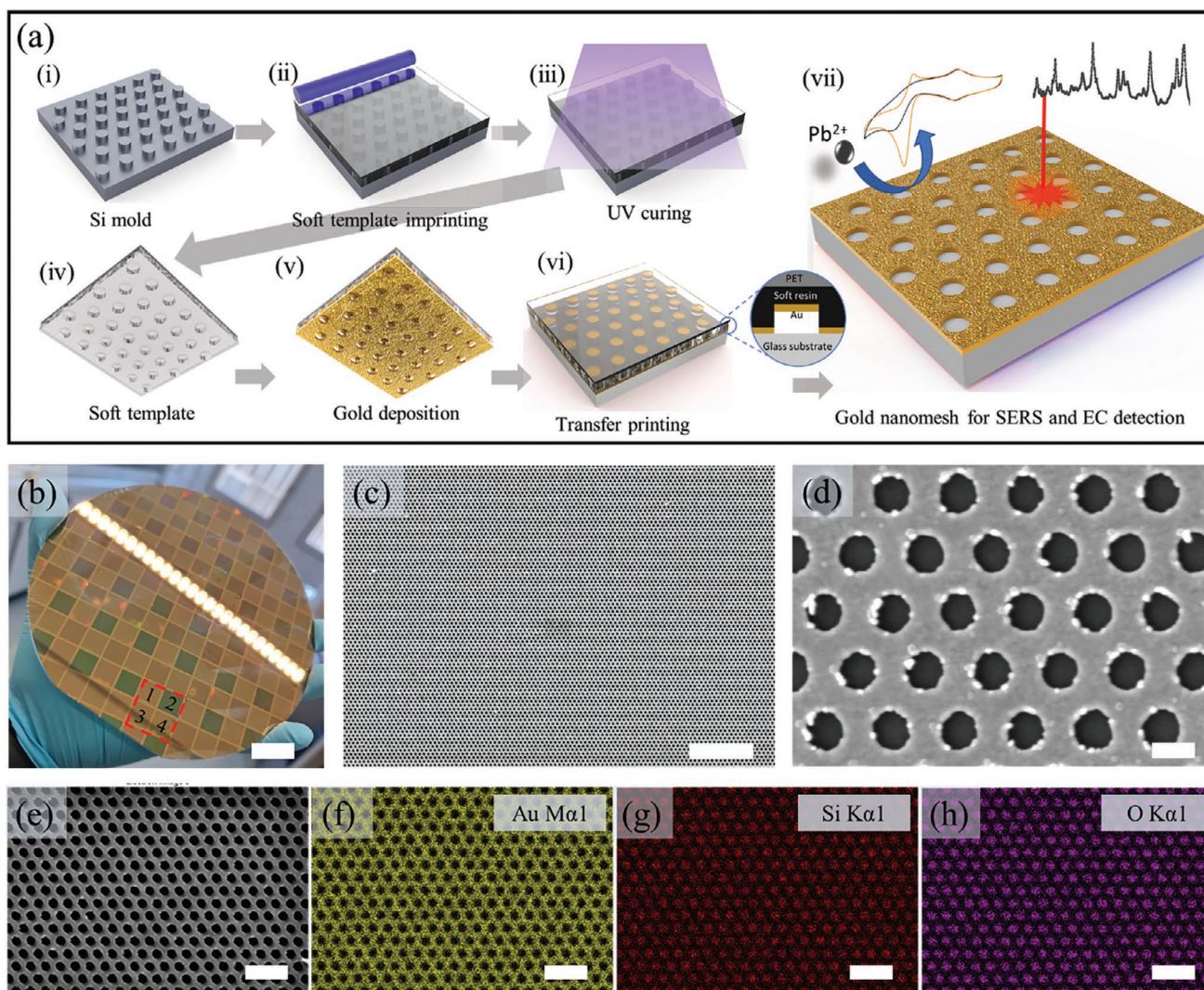
Figure 1. Schematics and structural characterization. a) Schematic illustration for the fabrication process of the AuNM multiplex sensing substrate: (i) Si hard mold, (ii) inverse soft template by imprinting process, (iii) UV curing for soft template formation, (iv) detachment of soft template, (v) gold deposition, (vi) transfer printing onto glass substrate, and (vii) AuNM on glass substrate for SERS and electrochemical detection. b) Photograph of the fabricated structures on a 6-inch glass wafer. Scanning electron microscope (SEM) images of region 2 with: c) a large area to demonstrate the uniformity and d) a close-up view of the AuNM structure with nanohole size about 170 nm. e) The structural image, and corresponding element mapping of: f) gold, g) silicon, and h) oxygen for the AuNM structures. Scale bar sizes are: (b) 2 cm, (c) 5 µm, (d) 200 nm, and (e–h) 1 µm.

assist to amplify the Raman-scattering effect, enhance the characteristic Raman fingerprint signal of target components, and thus improve the signal-to-noise ratio toward lower analyte concentration detection. Rhodamine 6G (R6G), which is a commonly used prototype molecule to indicate the SERS effect, is first utilized to demonstrate the SERS effect of the fabricated AuNM. AuNM structures in region 1 are used together with 785 nm laser source out of a screening test as illustrated in Figure S4 (Supporting Information). The R6G Raman spectra of the fabricated AuNM structures, where a 1 mm × 1 mm square chip is first treated by a mild oxygen plasma and then dropcasted by 40 µL R6G with a concentration of 1 mM, has been illustrated in **Figure** 2a. To quantitatively show how much the Raman signal is amplified by AuNM, samples with 50-nm-thick continuous gold film on the same glass substrate deposited by electron beam evaporation are employed as the references. A high

concentration of R6G is used, so that a weak but clear signal can be obtained even from the reference sample for a meaningful caparison (the reference signal as denominator is not close to zero). From these experiments, a significantly amplified signal of the Raman scattering has been observed, which is assumed to be induced by the strong plasmon resonance and enhanced electrical field at the edge of nanoholes.

The average enhancement factor (AEF), as a quantitative indicator, was calculated to represent the level of signal amplification attributable to the AuNM structure by the following equation: $AEF = I_{mesh}/I_{film}$, where I_{mesh} and I_{film} are the Raman intensities at 1360 cm^{-1} on the AuNM and the Au film substrates, respectively. The calculated AEF value is about 488.4, indicating more than two orders amplification excited by the nanomesh pattern. To check the SNRs of each case, these data from 850 to 950 cm^{-1} are used as the background to calculate
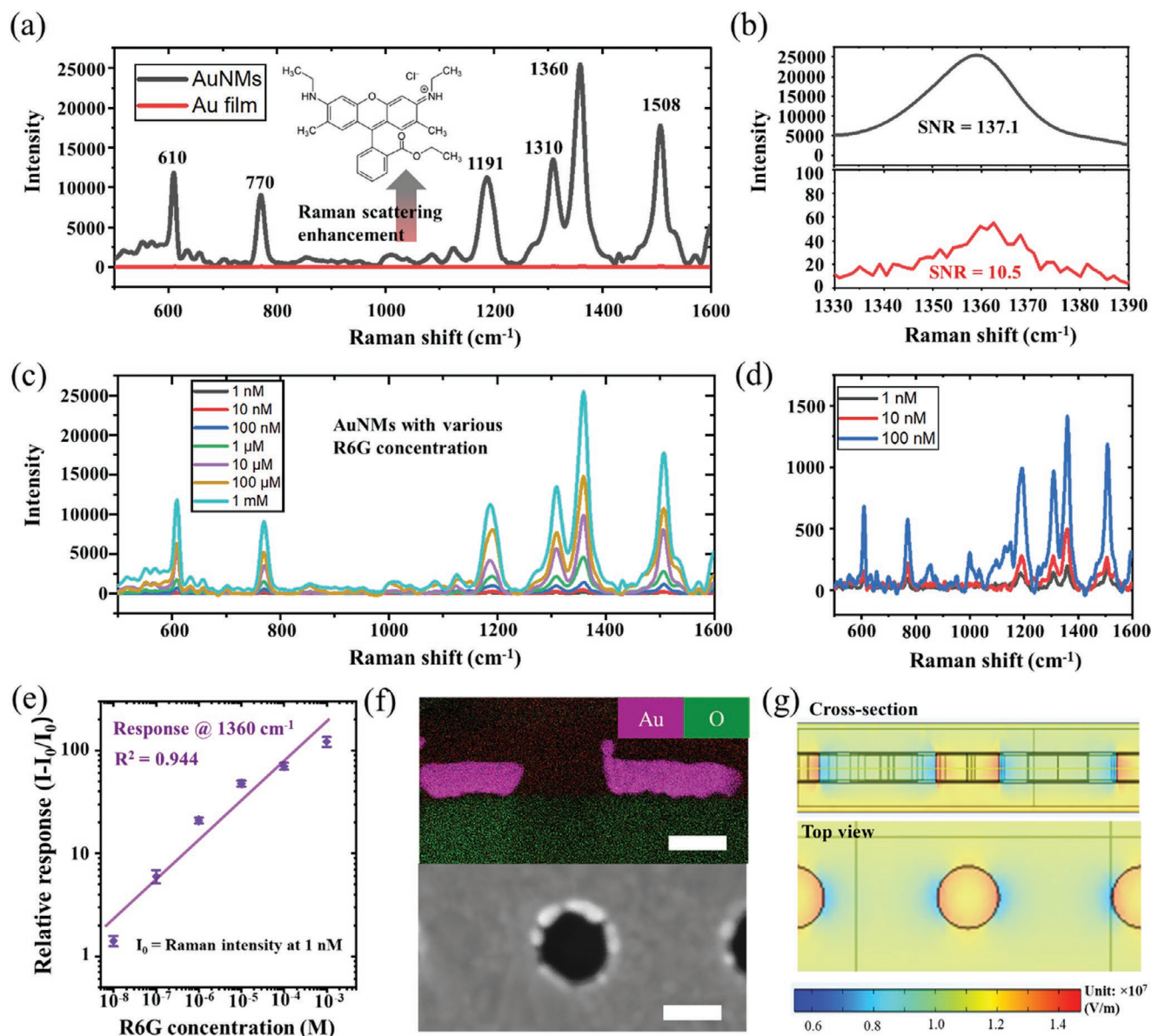
**ADVANCED
SCIENCE NEWS**

www.advancedsciencenews.com

**ADVANCED
MATERIALS
TECHNOLOGIES**

www.advmattechnol.de

Figure 2. Characterization of AuNM as SERS substrates. a) Raman spectra (500 to 1600 cm⁻¹) of 1 mM R6G with both AuNM and Au-film SERS substrates as a standard characterization of SERS effect, indicating a significant enhancement of Raman scattering effect by the AuNM. b) Close-up view of the Raman signal from (a) at Raman shift of 1360 cm⁻¹, showing the larger signal-to-noise ratio of the AuNM SERS substrates. c) Raman spectra (500 to 1600 cm⁻¹) of R6G with concentration from 1 nM to 1 mM and d) Zoom-in view for the response to R6G with concentration from 1 to 100 nM. e) Relative Raman response ($I–I_0/I_0$, where I_0 is the Raman intensity of 1 nM) at 1360 cm⁻¹ with different R6G concentrations, where both x and y axes are in logarithm scale. f) The corresponding TEM image and SEM image indicating the dimension of the AuNM utilized, where the scale bars are 100 nm. g) Numerical simulation of the locally magnified electrical field distribution of AuNM structures upon the excitation at 785 nm.

the standard deviation of the data. Here, we simply define the SNR as the ratio between the peak value at 1360 cm⁻¹ to the calculated standard deviation. The value obtained with 1 mM R6G on the AuNM is about 137.1, which is significantly higher than 10.5 obtained from the Au film reference sample. These results verified that our AuNM SERS substrates amplified not only the absolute signal but also enabled larger SNRs.

To demonstrate the SERS performance of AuNM in a suitable dynamic range, R6G concentration from 1 nM to 1 mM is utilized and the Raman spectra are exhibited in Figure 2c. The results show distinguishable responding intensities with

various concentrations. The zoom-in view for those low concentration responses is illustrated in Figure 2d, which shows clear response even down to 1 nM condition. The relationships between the relative Raman intensity and the R6G concentration using the peak values 1360 cm⁻¹ are plotted in Figure 2e, and that of other Raman peak positions are illustrated in Figure S5 (Supporting Information). Strong linear relationships under the log–log scale are observed from the experimental results. Furthermore, an area of 40 μm × 40 μm was scanned with 25 points in total and the results are illustrated in Figure S6 (Supporting Information). Those points give an average

intensity of 4185 and standard deviation of 305, which can be converted into a relative error value of 0.729, indicating a good uniformity regarding the SERS response of AuNM substrate. Based on the dimensional features measured from the SEM and TEM in Figure 2f, we further conduct numerical simulation to check the excited electrical field distribution of the AuNM under the 785-nm laser illumination. The simulation results are shown in Figure 2g, which indicates magnified local plasmonic field near the nanohole edge. The computational results of the plasmonic enhanced light-matter interaction and constructed strong near-fields demonstrated that the AuNMs subtracted the leveraged electromagnetic enhancement mechanism to achieve the satisfactory SERS.[28]

2.3. AuNM-Based SERS toward DNA Nucleotide Detection

To further demonstrate the potential SERS-based applications toward biochemical substrances detection, four types of deoxyribonucleotide triphosphates (dNTPs) and a representative DNA sequence are employed for the SERS detection on the AuNM substrates. The capability of the SERS substrates, which can effectively enhance the intrisic Raman signals of different dNTPs is of importance, since it can be useful in monitoring various biological processes.[29] For instance, the adenosine dephosphorylation is a common chemical phenomenon occurring during cell "hijacking" machinery of viruses.[30] The testing methods are similar with those used for R6G characterization above, with more detailed explanation in the Experimental section.

The molecular structures and correspondding Raman spectra of dTTPs, dCTPs, dGTPs, and dATPs are illustrated in **Figure 3**a. These dNTPs show some shared Raman features due to the structural similarity. The Raman signals originating from C to N vibration in the nitrogenous bases appear in all dNTPs, generally located from 1100 to 1500 cm^{-1}. These peak shifts among the four dNTPs are caused by different bond conditions in each of them.[31] In contrast, the C=N bond vibrations located from 1500 to 1600 cm^{-1} in dATPs, dGTPs, and dCTPs are not found in dTTPs. These major peaks acting as potential characterization fingerprint bands are marked accordingly. Taking the spectrum of dATPs as an example, strong features appear at 668, 732, 1338, and 1471 cm^{-1}. Although some of these peaks overlap with those from other dNTPs, the whole Raman spectral patterns still show various specific characteristics, as illustrated in Figure 3a. The Raman spectra of the dNTPs with 1 nM concentration on the substrate are also measured, and the results indicate that the distinguishable signals can still be obtained at this low concentration (Figure S7, Supporting Information). A close-up view of Raman spectra from 600 to 800 cm^{-1} of dATP with concentration from 1 nM to 10 μM was plotted in Figure S8 (Supporting Information), indicating good dynamic response of AuNM substrates.

A synthesized single-strand DNA (ssDNA) without thymine (T) is then tested on our AuNM SERS substrates, to further prove the potential capability of distinguishing the signal from a mixture of those dNTPs. The ssDNA used is composed of adenine (A), cytosine (C), and guanine (G) with a sequence as AAC-AAA-CGC-CAG-GAA-GAG. Dominant Raman fingerprints of A are clearly observed at 668, 732, 1338, and 1471 cm^{-1}. Strong C peaks at 783 and 1293 cm^{-1} are also clearly identified in the mixture spectrum. G peaks overlap with A at 1341 and 1479 cm^{-1}, while the additional signal at 1578 cm^{-1} confirms the existence of G within the tested ssDNA. The major T peaks are absent that agree with the fact that no T appears in the ssDNA. Although this preliminary experiment only shows the qualitative analysis of the nucleotides, more quantitative analysis is promising with the rapid advancement of various data technology.[32–34]

2.4. AuNM-Based Electrochemical Detection of Metal Ions

Figure 4a shows that the AuNM electrodes provide a potential window from 0 to more than 1.2 V versus the reversible hydrogen electrode (RHE) in the electrolyte (0.1 M acetate buffer). The onset voltages of oxygen reduction and hydrogen evolution are about 0.45 and 0 V, respectively, while the oxidation and reduction peaks in 20 μM Pb^{2+} solution are at about 0.45 and 0.4 V, respectively. Prior to the determination of Pb^{2+} using the AuNM electrodes, the square wave anodic stripping voltammetry (SWASV) parameters are optimized, to enhance the signals by increasing the current peaks and peak sharpness, and the parameter optimization details are characterized in Figure S9 (Supporting Information). The significant hydrogen evolution has a minor effect on the current peaks, which become stable with a deposition potential more negative than 0.2 V (Figure S9a, Supporting Information). Figure S9b (Supporting Information) indicates that the current peak increases by up to 30% with higher pulse widths. The peak sharpness is an important factor influencing the resolution of the current peak and possible current peaks overlap, so the full width at half-maximum (FWHM) is introduced to select optimal values of stripping step potential and voltammetry (SW) amplitude (Figure S9c,d, Supporting Information). The step potential has a minor influence on the current peaks (Figure S9c, Supporting Information), whereas higher SW amplitudes lead to higher current peaks (Figure S9d, Supporting Information). In contrast, a higher SW amplitude and step potential result in a higher FWHM that indicates a poorer peak resolution. Overall, 0 V, 9 ms, 5 mV, and 35 mV are found to be the optimized testing parametric values for deposition potential, pulse width, step potential, and SW amplitude, respectively.

As illustrated in Figure 4b, Pb^{2+} with concentration from 30 to 1000 nM are tested with those optimized parameters discussed above. The results indicate a strong linear relationship between the measured current peak and Pb^{2+} concentration within the test dynamic range (Figure 4c). These results illustrate that the limit of detection of the electrode was about 30 nM for quantifying the standard Pb^{2+} solution. Here, the limit of detection is defined as the ratio of the threefold standard deviation of the background value to the curve slope (current peak/Pb concentration). The electrode selectivity is later examined by testing and calculating the changes in the peak current in Pb^{2+} solutions added with other metal ions. In this interference study, we select Ca^{2+}, Fe^{3+}, Zn^{2+}, and Cd^{2+} as the interfering ions and the concentration of interfering ions is ten times higher than the tested Pb^{2+} concentrations. The final
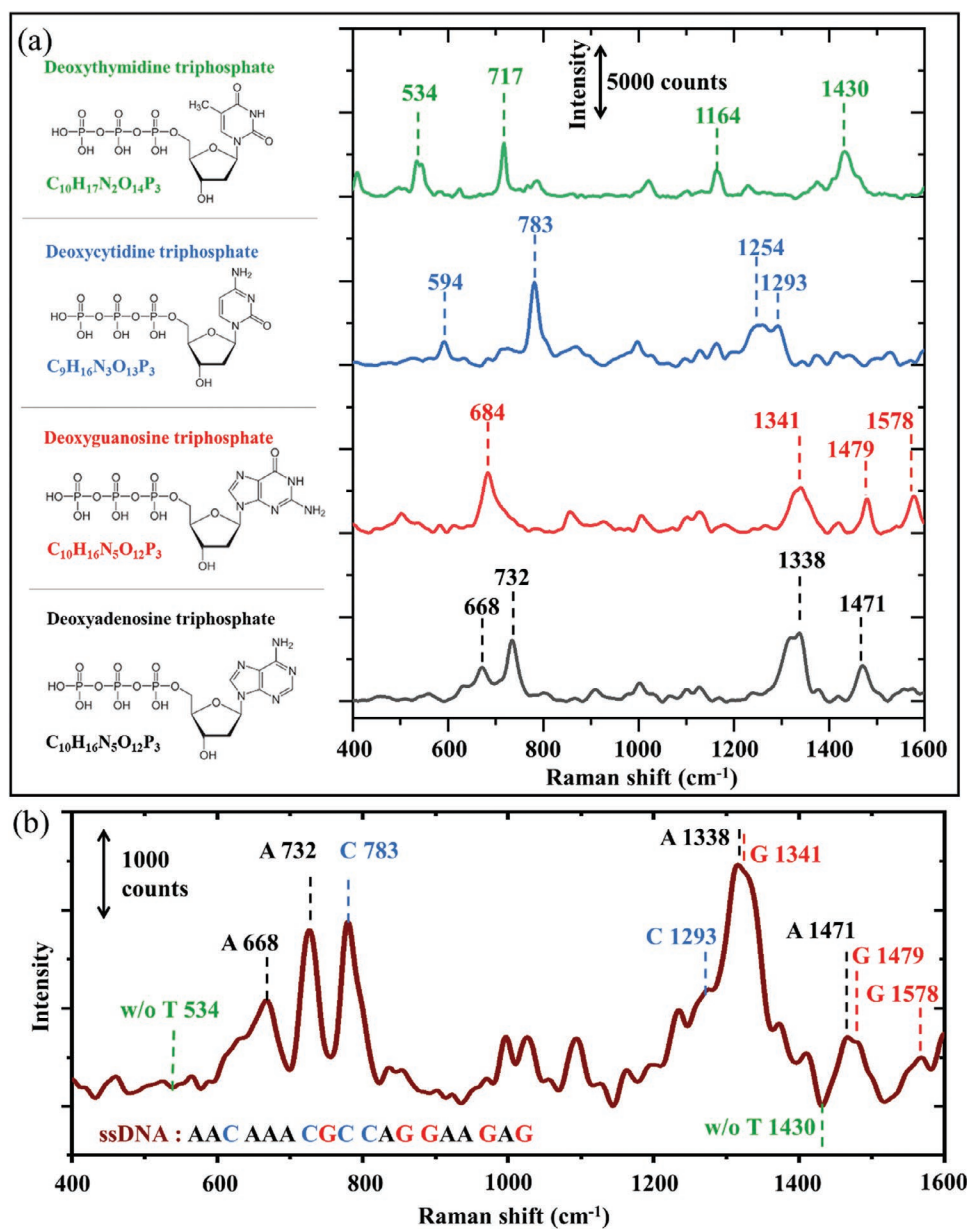
Figure 3. Raman spectra of deoxyribonucleotide triphosphates (dNTPs) and DNA sequence. a) Molecular structures of deoxythymidine triphosphate (dTTP), deoxycytidine triphosphate (dCTP), deoxyguanosine triphosphate (dGTP) and deoxyadenosine triphosphate (dATP), and their corresponding Raman spectra. b) Raman spectrum of a single-strand DNA sequence without thymine (AAC-AAA-CGC-CAG-GAA-GAG). The dNTPs and ssDNA solution used in this figure are 10 and 1 µM, respectively.

results are exhibited in Figure 4d by using the detection ratio, which indicates the ratio of signals with the interfering ions to that without the interfering ions in the electrolyte. In general, Ca^{2+} and Fe^{3+} show a negligible effect on the current peaks, whereas Zn^{2+} and Cd^{2+} decrease the current peak of Pb on average by 14.84% and 19.05%, respectively. Such minor deterioration is likely due to the reason that Zn^{2+} and Cd^{2+} might compete with Pb^{2+} to occupy electroactive sites on the AuNM electrode surface. Overall, our AuNM shows the good capability to selectively detect the Pb^{2+} out of a mixture with higher concentration interfering ions. Compared with other works on

Pb^{2+} sensing,[35,36] a comparable limit of detection was achieved without modifications on our nanomesh electrode, which also indicated great potential to further improve the limit of detection with novel modification strategies based on the proposed electrode. In addition, a wider linear range makes it a practical platform to measure samples containing Pb^{2+} with different concentrations.

Further comparison on recently reported SERS/EC dual-mode sensing platforms regarding structures, fabrication methods, target analytes, lower limit of detection, and linear working range is illustrated in **Table 1**. On the whole, our
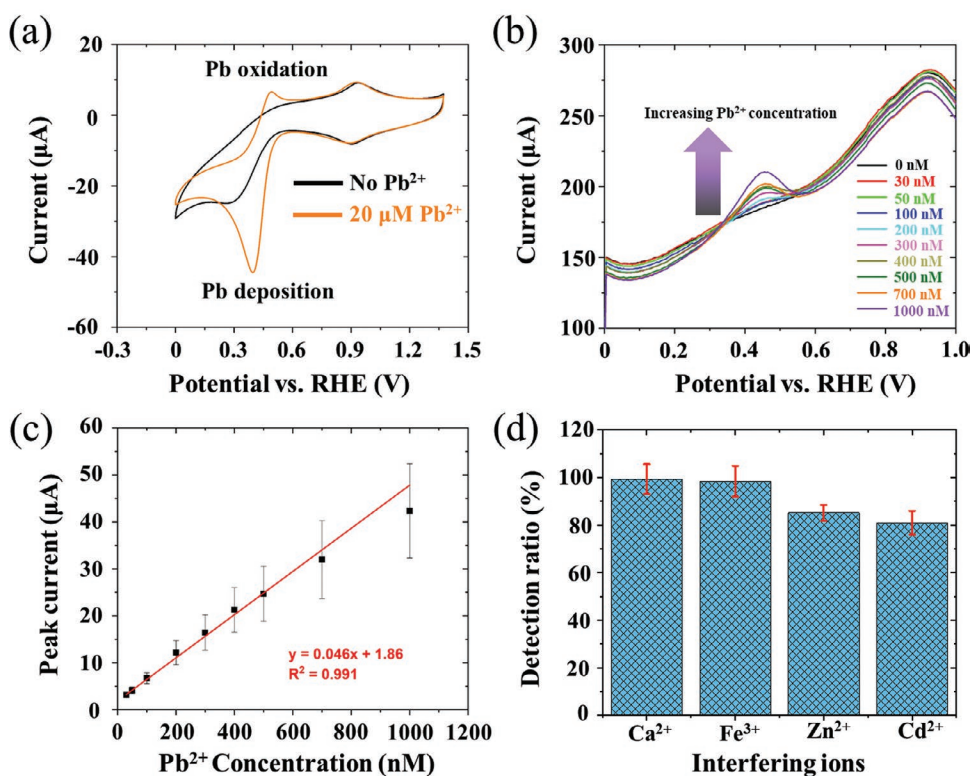
Figure 4. Electrochemical detection of metallic ions using AuNM as working electrodes. a) Cyclic voltammetry of the AuNM serving as the working electrode at sweeping 100 mV s^{-1} in a 20 μM Pb^{2+} environment (pH 4.45) and under the same conditions but without Pb^{2+}, where the Pt reference electrode and Ag/AgCl (3 M KCl) counter electrode are used. b) Current peaks from the electrochemical response of AuNM electrodes using the square wave anodic-stripping voltammetry methods with optimized parameters (deposition potential: 0 V, deposition time: 150 s, stripping voltammetry: 35 mV, step potential: 5 mV, pulse width: 9 ms). c) Calibration curve of the SWASV peak current in response to Pb^{2+} with concentration from 0 nM to 1 μM, which indicates the linear relationship between the electrochemical response and Pb^{2+} concentration within the tested range. d) Selectivity test of the AuNM electrodes toward 1 μM Pb^{2+} containing individually 10 μM Ca^{2+}, Fe^{3+}, Zn^{2+}, and Cd^{2+} interfering ions, where the detection ratio indicates the ratio of signals with the interfering ions to that without the interfering ions in the electrolyte.

AuNM-based devices demonstrate cost-efficient wafer-scale fabrication capability while still deliver comparable sensing performance regarding SERS measurements as well as electrochemical sensing. Meanwhile, our wafer-scale NIL fabrication process via the top–down route shows advantage regarding the structural diversity and property tunability.

3. Conclusion

In summary, we reported wafer-scale, uniformly patterned AuNM structures on glass substrates with 100-nm scale features via nanoimprinting and secondary chemisorption-assisted transfer printing technology. Compared with the conventional

Table 1. Comparison on recently reported SERS/EC dual-mode sensing platform.

Structures	Fabrication	Analytes	LoDs	Linear range	Ref.
AgNWs	Hydrothermal	H$_2$O$_2$	0.1 mM	0.1–5.3 mM	Ref. [37]
Au/graphene	Electrodeposition	miRNA	0.1 pM	0.1 pM–1 nM	Ref. [38]
Ag/Au	Electrodeposition	Riboflavin	1 nM SERS 100 nM EC	Not reported	Ref. [39]
AgNPs	Electrodeposition	Chlorfenapyr	4.2 ppm	20–50 ppm	Ref. [40]
Au/SiNWs	Chemical vapor deposition	Avidin	1 nM SERS10 pM EC	Not reported	Ref. [41]
WO$_3$/SnO$_2$	Hydrothermal	Dopamine	1.5 nM SERS 0.8 nM EM	5 nM–1.7 μM	Ref. [42]
Au/SiO$_2$	Reactive ion etching	Paracetamol	30 uM	30 μM–3 mM	Ref. [43]
AuNMs	Nanoimprinting lithography	dNTPs	1 nM	1 nM–10 μM	This work
		Pb^{2+}	30 nM	30 nM–1 μM	

fabrication methods for achieving such a small dimension, our approach is cost-efficient and suitable for mass production. The fabricated AuNM is then utilized as SERS substrates for enhancing the Raman spectra and working electrodes of electrochemical system for certain detection metal ions, demonstrating the various potential applications toward biochemical substance detection. In SERS sensing mode, different nucleotides can be detected down to 1 nM level and distinguished via their unique fingerprint patterns. As for electrochemical analysis mode, Pb^{2+} ions can be detected out of other interfering components with the concentration down to 30 nM. As an optical analytical method, SERS provides fingerprint identification of the analytical molecules in a label-free and nondestructive way. On the other hand, electrochemical methods can be responsive to those metallic analytes without Raman scattering effects. Overall, our proposed cost-effective fabrication method and multiple sensing capabilities allow our approach to be scaled up to produce low-cost, high-performance sensors. In addition, the fabricated sensors can be used to selectively and sensitively detect biochemicals through different sensing mechanisms, which show potential for a wide range of applications, such as wearable electronic devices, smart POC diagnostics, IoTs, and environmental monitoring. Moreover, by diversifying the materials and structures employed, further opto-electrical sensing mechanism and devices can be explored.

4. Experimental Section

Fabrication Process: Si hard templates consisting of the nanopillar patterns were fabricated via the conventional KrF photolithography process with the initial mask patterns and those patterns were transferred to Si by further reactive ion etching (RIE). The fabricated Si templates were then treated by self-assembled monolayers (SAMs) consisting of trichloro(1H,1H,2H,2H-perfluoroocty) silane (Sigma-Aldrich) at 80 °C for 0.5 h, to reduce the adhesion between the hard templates and the inverse structures of polymers casted on them. Polymer resins of RM-311 (Minuta Technology Co., Ltd., Korea; polyurethane) were used as the soft template materials, with its low surface energy. The resin was coated on a polyethylene terephthalate (PET) substrate and then covered with the Si hard templates. Uniform pressure was applied by a roller for good uniformity. UV curing was followed to fully polymerize the resins. The polymer template could be detached and used for the later transfer process. Au layer was deposited on the soft polymer template by electron beam evaporation with a deposition rate about 1 Å s^{-1}. The transfer printing process was conducted using a thermal imprinting system (Hutem Co., Korea). The glass wafer receiving substrates were precoated with a chemical adhesion layer (*N*-[3-(trimethoxysilyl)propyl]ethylenediamine) and then attached with the polymer template at 5 bar, 160 °C for 5 min to transfer the AuNM pattern from polymer template to glass substrates. The final AuNM on glass substrates was then diced into 1 mm × 1 mm chips for later sensing experiments. Region 1 was used in the following sensing experiments in this work.

Electron Microscope Characterization: The AuNM structures were characterized using a scanning electron microscope (SEM) SU-5000 (Hitachi, Japan) and a transmission electron microscope (TEM) Talos F200X (Thermo Fisher Scientific, the Netherlands) with a Super-X EDS system (Bruker, US) at STEM mode operating at 200 kV.

Theoretical Modeling of Plasmonic Near-Fields of AuNMs: The plasmonic near-fields were simulated by the Finite element method (FEM) based on the commercial software COMSOL (MA, USA). The Wave Optics Module was used to simulate the output spectra and electromagnetic field profiles for the proposed AuNM structures. The

energy density represented by the electrical field intensity of the incident 785 nm light was set to 1 V m^{-1}.

Raman Spectra Measurement: The Raman spectra were measured using Raman spectroscopy (LabRAM HR Evolution UV-VIS-NIR, Horiba, Japan). Samples (AuNM and Au films) were pretreated with a mild oxygen plasma at 15 W for 1 min to increase the surface wettability. The 40 µL prepared aqueous solutions containing certain concentration of target analytes (R6G, dNTPs, and ssDNA) were then dropped onto the sample substrates with size of 1 mm × 1 mm. The samples were dried before checking the Raman signals. For detection, a 785-nm high-power signal frequency diode laser (Toptica XTRA II) source was used to excite the Raman signal, where 3 mW laser power were used. A 100× objective (Nikon) was used for the microprobe sampling. The obtained Raman spectra were accumulated for 30 s and averaged for three times each. Baseline corrections of the raw Raman spectra were conducted using Labspec 6.5. The dNTPs and ssDNA solution used in Figure 3 were 10 and 1 µM, respectively. dNTPs with concentration down to 1 nM were also measured and illustrated in Supporting Information.

Electrochemical Measurement: The Pb oxidation peak and the potential window of the electrodes were determined using Cyclic voltammetry (CV) conducted in 0.1 M acetate buffer (pH 4.45) with a scan rate of 100 mV s^{-1}. The roughness factors of the electrodes were acquired by calculating the gold oxidation peak in the 0.5 M H_2SO_4 solution and 390 µC cm^{-2} was applied as the conversion factor. It was found that the roughness factors of electrodes with different structures were similar, with an average value of 1.95 ± 0.26, which indicated that the specific structures enhanced the specific area. SWASV was the electrochemical technique to measure the Pb concentrations in the liquid phase without removing dissolved oxygen. The deposition and stripping parameters involved in SWASV including pulse width, SW amplitude, and step potential were optimized prior to the determination of Pb^{2+} concentrations. The calibration and interference studies were conducted by randomly choosing three electrodes to determine the working concentration ranges and detection ratios, respectively.

Supporting Information

Supporting Information is available from the Wiley Online Library or from the author.

Acknowledgements

Conflict of Interest

The authors declare no conflict of interest.

[1] R. A. Potyrailo, *Chem. Rev.* **2016**, *116*, 11877.

[2] R. Byrne, D. Diamond, *Nat. Mater.* **2006**, *5*, 421.

[3] H. K. Hunt, A. M. Armani, *Nanoscale* **2010**, *2*, 1544.

[4] Y. Cui, Q. Wei, H. Park, C. M. Lieber, *Science (1979)* **2001**, *293*, 1289.

[5] N. Barsan, U. Weimar, *J. Electroceramics* **2001**, *7*, 143.

[6] G. Qiu, Z. Gai, Y. Tao, J. Schmitt, G. A. Kullak-Ublick, J. Wang, *ACS Nano* **2020**, *14*, 5268.

[7] A. G. Brolo, *Nat. Photon.* **2012**, *6*, 709.

[8] M. I. Mead, O. A. M. Popoola, G. B. Stewart, P. Landshoff, M. Calleja, M. Hayes, J. J. Baldovi, M. W. McLeod, T. F. Hodgson, J. Dicks, A. Lewis, J. Cohen, R. Baron, J. R. Saffell, R. L. Jones, *Atmos. Environ.* **2013**, *70*, 186.

[9] A. J. Bandodkar, J. Wang, *Trends Biotechnol.* **2014**, *32*, 363.

[10] A. Mujahid, A. Afzal, F. L. Dickert, *Sensors* **2019**, *19*, 4395.

[11] J. Zhang, X. Zhang, X. Wei, Y. Xue, H. Wan, P. Wang, *Anal. Chim. Acta* **2021**, *1164*, 338321.

[12] C. Jianrong, M. Yuqing, H. Nongyue, W. Xiaohua, L. Sijiao, *Biotechnol. Adv.* **2004**, *22*, 505.

[13] M. Gao, Z. J. Zhao, H. Kim, M. Jin, P. Li, T. Kim, K. Kang, I. Cho, J. H. Jeong, I. Park, *ACS Appl. Mater. Interfaces* **2020**, *12*, 37128.

[14] H. Kim, J. Yun, M. Gao, H. Kim, M. Cho, I. Park, *ACS Appl. Mater. Interfaces* **2020**, *12*, 43614.

[15] L. Liu, Y. Wang, F. Sun, Y. Dai, S. Wang, Y. Bai, L. Li, T. Li, T. Zhang, S. Qin, *Microsyst. Nanoeng.* **2020**, *6*, 31.

[16] Y. W. Chang, R. G. Liu, S. Y. Fang, *Proc. of the 52nd Annual Design Automation Conf.*, June **2015**, https://doi.org/10.1145/2744769.2747925.

[17] K. Ariga, *Nanoscale Horiz.* **2021**, *6*, 364.

[18] I. Gunkel, *Small* **2018**, *14*, 1802872.

[19] Z. Wang, B. Ai, H. Möhwald, G. Zhang, Z. Wang, G. Zhang, B. Ai, H. Möhwald, *Adv. Opt. Mater.* **2018**, *6*, 1800402.

[20] M. Gao, M. Cho, H. J. Han, Y. S. Jung, I. Park, *Small* **2018**, *14*, 1703691.

[21] Z. J. Zhao, M. Gao, S. H. Hwang, S. Jeon, I. Park, S. H. Park, J. H. Jeong, *ACS Appl. Mater. Interfaces* **2019**, *11*, 7261.

[22] Z. J. Zhao, S. H. Shin, S. Y. Lee, B. Son, Y. Liao, S. Hwang, S. Jeon, H. Kang, M. Kim, J. H. Jeong, *ACS Nano* **2022**, *16*, 378.

[23] Z. J. Zhao, J. Ahn, S. H. Hwang, J. Ko, Y. Jeong, M. Bok, H. J. Kang, J. Choi, S. Jeon, I. Park, J. H. Jeong, *ACS Nano* **2021**, *15*, 503.

[24] Z. J. Zhao, J. Ko, J. Ahn, M. Bok, M. Gao, S. H. Hwang, H. J. Kang, S. Jeon, I. Park, J. H. Jeong, I. Park, J. H. Jeong, *ACS Sens.* **2020**, *5*, 2367.

[25] H. J. Han, S. H. Cho, S. Han, J. S. Jang, G. R. Lee, E. N. Cho, S. J. Kim, I. D. Kim, M. S. Jang, H. L. Tuller, J. J. Cha, Y. S. Jung, *Adv. Mater.* **2021**, *33*, 2105199.

[26] R. Moldovan, E. Vereshchagina, K. Milenko, B. C. Iacob, A. E. Bodoki, A. Falamas, N. Tosa, C. M. Muntean, C. Farcău, E. Bodoki, *Anal. Chim. Acta* **2022**, *1209*, 339250.

[27] S. H. Hwang, S. Jeon, M. J. Kim, D. G. Choi, J. H. Choi, J. Y. Jung, K. S. Kim, J. Lee, J. H. Jeong, J. R. Youn, *Nanoscale* **2017**, *9*, 14335.

[28] P. L. Stiles, J. A. Dieringer, N. C. Shah, R. P. van Duyne, *Annu. Rev. Anal. Chem* **2008**, *1*, 601.

[29] G. Pezzotti, *J. Raman Spectrosc.* **2021**, *52*, 2348.

[30] F. Keck, P. Ataey, M. Amaya, C. Bailey, A. Narayanan, *Viruses* **2015**, *7*, 5257.

[31] F. D'Amico, F. Cammisuli, R. Addobbati, C. Rizzardi, A. Gessini, C. Masciovecchio, B. Rossi, L. Pascolo, *Analyst* **2015**, *140*, 1477.

[32] J. A. Valeri, K. M. Collins, P. Ramesh, M. A. Alcantar, B. A. Lepe, T. K. Lu, D. M. Camacho, *Nat. Commun.* **2020**, *11*, 5058.

[33] P. H. L. Nguyen, B. Hong, S. Rubin, Y. Fainman, *Biomed. Opt. Express* **2020**, *11*, 5092.

[34] X. Zheng, S. Xu, Y. Zhang, X. Huang, *Sci. Rep.* **2019**, *9*, 628.

[35] S. Dutta, G. Strack, P. Kurup, *Sens. Actuators B Chem.* **2019**, *281*, 383.

[36] I. Albalawi, A. Hogan, H. Alatawi, E. Moore, *Sens. Biosensing Res.* **2021**, *34*, 100454.

[37] Y. C. Chen, J. H. Hsu, Y. G. Lin, Y. K. Hsu, *Sens. Actuators B Chem.* **2017**, *245*, 189.

[38] H. Zhou, J. Zhang, B. Li, J. Liu, J. J. Xu, H. Y. Chen, *Anal. Chem.* **2021**, *93*, 6120.

[39] M. R. Bailey, A. M. Pentecost, A. Selimovic, R. S. Martin, Z. D. Schultz, *Anal. Chem.* **2015**, *87*, 4347.

[40] J. Liu, R. Siavash Moakhar, S. Mahshid, F. Vasefi, S. Wachsmann-Hogiu, *Appl. Surf. Sci.* **2021**, *566*, 150617.

[41] A. Convertino, V. Mussi, L. Maiolo, *Sci. Rep.* **2016**, *6*, 25099.

[42] L. Lu, Y. Zhou, T. Zheng, Y. Tian, **2022**, https://doi.org/10.1007/s12274-022-4984-0.

[43] K. Sanger, O. Durucan, K. Wu, A. H. Thilsted, A. Heiskanen, T. Rindzevicius, M. S. Schmidt, K. Zór, A. Boisen, *ACS Sens.* **2017**, *2*, 1869.